



Cite as
Nano-Micro Lett.
(2019) 11:101

Received: 23 September 2019
Accepted: 23 October 2019
Published online: 20 November 2019
© The Author(s) 2019

All Binder-Free Electrodes for High-Performance Wearable Aqueous Rechargeable Sodium-Ion Batteries

Bing He^{1,3,4}, Ping Man^{1,3}, Qichong Zhang⁵, Huili Fu^{1,3}, Zhenyu Zhou^{1,3}, Chaowei Li^{1,3}, Qiulong Li^{1,2}, Lei Wei⁵, Yagang Yao^{1,2,4} ✉

Bing He and Ping Man contributed equally to this work.

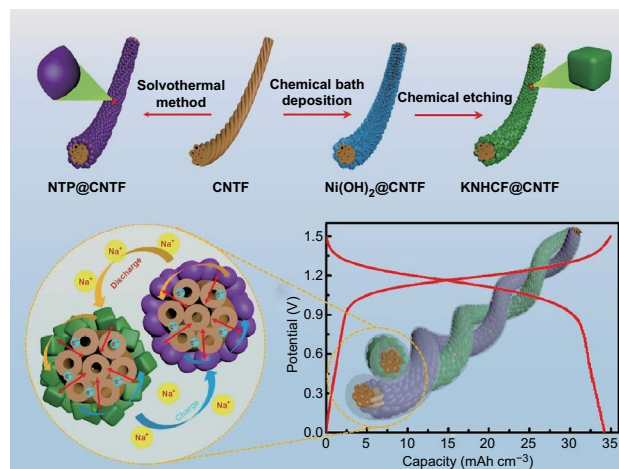
✉ Yagang Yao, ygyao2018@nju.edu.cn

- ¹ Division of Advanced Nanomaterials, Key Laboratory of Nanodevices and Applications, Joint Key Laboratory of Functional Nanomaterials and Devices, CAS Center for Excellence in Nanoscience, Suzhou Institute of Nano-Tech and Nano-Bionics, Chinese Academy of Sciences, Suzhou 215123, People's Republic of China
- ² National Laboratory of Solid State Microstructures, College of Engineering and Applied Sciences, Jiangsu Key Laboratory of Artificial Functional Materials, and Collaborative Innovation Center of Advanced Microstructures, Nanjing University, Nanjing 210093, People's Republic of China
- ³ School of Nano Technology and Nano Bionics, University of Science and Technology of China, Hefei 230026, People's Republic of China
- ⁴ Division of Nanomaterials, Suzhou Institute of Nano-Tech and Nano-Bionics, Nanchang, Chinese Academy of Sciences, Nanchang 330200, People's Republic of China
- ⁵ School of Electrical and Electronic Engineering, Nanyang Technological University, 50 Nanyang Avenue, Jurong West 639798, Singapore

HIGHLIGHTS

- Nanocube-like KNiFe(CN)₆ and rugby ball-like NaTi₂(PO₄)₃ are grown on carbon nanotube fibers via simple and mild methods.
- A quasi-solid-state fiber-shaped aqueous rechargeable sodium-ion battery based on all binder-free electrodes is successfully assembled for the first time, delivering a high volumetric capacity of 34.21 mAh cm⁻³ and impressive volumetric energy density of 39.32 mWh cm⁻³.
- The device delivers superior mechanical flexibility with only 5.7% of initial capacity loss after bending at 90° for over 3000 cycles.

ABSTRACT Extensive efforts have recently been devoted to the construction of aqueous rechargeable sodium-ion batteries (ARSIBs) for large-scale energy-storage applications due to their desired properties of abundant sodium resources and inherently safer aqueous electrolytes. However, it is still a significant challenge to develop highly flexible ARSIBs ascribing to the lack of flexible electrode materials. In this work, nanocube-like KNiFe(CN)₆ (KNHCF) and rugby ball-like NaTi₂(PO₄)₃ (NTP) are grown on carbon nanotube fibers via simple and mild methods as the flexible binder-free cathode (KNHCF@CNTF) and anode (NTP@CNTF), respectively. Taking advantage of their high conductivity, fast charge transport paths, and large accessible surface area, the as-fabricated binder-free electrodes display admirable



electrochemical performance. Inspired by the remarkable flexibility of the binder-free electrodes and the synergy of KNHCF@CNTF and NTP@CNTF, a high-performance quasi-solid-state fiber-shaped ARSIB (FARSIB) is successfully assembled for the first time. Significantly, the as-assembled FARSIB possesses a high capacity of $34.21 \text{ mAh cm}^{-3}$ and impressive energy density of $39.32 \text{ mWh cm}^{-3}$. More encouragingly, our FARSIB delivers superior mechanical flexibility with only 5.7% of initial capacity loss after bending at 90° for over 3000 cycles. Thus, this work opens up an avenue to design ultraflexible ARSIBs based on all binder-free electrodes for powering wearable and portable electronics.

KEYWORDS Carbon nanotube fiber; Binder-free electrode; Flexibility; Aqueous rechargeable energy-storage device; Sodium-ion battery

1 Introduction

The ever-increasing demand for next-generation wearable electrical products has sparked a boom in the development of matched flexible energy-storage devices with high safety, lightweight, and remarkable biocompatibility [1–15]. In the past decade, sodium-ion batteries (SIBs) have emerged as a promising alternative to lithium-ion batteries, with which they share similar physicochemical properties, for large-scale electricity storage applications due to their abundant resources and low cost [16–21]. However, the conventional SIBs using flammable and toxic organic electrolytes are not suitable as wearable energy-storage devices [5, 22]. Encouragingly, aqueous electrolytes offer the significant advantages of low cost, high ion conductivity, and outstanding safety. It is thus stimulating intense studies on the development of aqueous rechargeable SIBs [5, 23–27]. Huang et al. developed an aqueous rechargeable SIB using flower-like $\text{K}_{0.27}\text{MnO}_2$ as the cathode and $\text{NaTi}_2(\text{PO}_4)_3$ (NTP) as the anode, exhibiting remarkable specific capacity and rate capacity [23]. Goodenough et al. reported a symmetric SIB with the sodium superionic conductor (NASICON)-structured $\text{Na}_3\text{MnTi}(\text{PO}_4)_3$ as both the anode and the cathode in an aqueous electrolyte, and it achieved a well-defined voltage plateau of about 1.4 V and excellent performance stability [24]. Very recently, Peng et al. firstly assembled flexible fiber-shaped ARSIBs (FARSIBs) ($\text{Na}_{0.44}\text{MnO}_2$ //NTP@C) with Na^+ -containing aqueous electrolytes, which delivered remarkable energy density and power density as well as good flexibility [5]. Despite the great progress achieved, all previously reported ARSIBs are fabricated based on powder electrode materials, whose electrode preparation is employed conventional slurry-casting techniques, thus leading to poor flexibility and inferior electrochemical performance [28, 29]. Note that the construction of self-standing active materials has been demonstrated as an effective way to develop

high-performance binder-free electrodes for energy-storage devices, which could provide excellent physical and chemical properties and strong adhesion between active materials and substrates for remarkable flexibility [30–32]. Nevertheless, there are few reports focusing on the preparation of binder-free electrodes for ARSIBs, which is attributed to the fact that the most common electrode materials for ARSIBs, such as M_xMnO_2 ($\text{M}=\text{K}, \text{Na}$), Prussian blue and its analogues (PBAs), and NTP, are unsuitable for direct growth on the collectors due to their preparation methods, including high-temperature solid-state, ball-milling, and coprecipitation methods [5, 23, 33–35]. Thus, developing effective and mild methods to fabricate binder-free cathodes and anodes is necessary for high-performance flexible ARSIBs.

PBAs have drawn considerable attention as advanced cathode materials for SIBs due to their open framework structure and large interstitial sites [33, 34, 36–39]. These features are extremely conducive to the intercalation and deintercalation of alkali cations with large ionic radius. However, it is difficult to form strong adhesion between the PBAs and current collectors by traditional coprecipitation methods. To address this problem, we adopt the chemical etching method to grow $\text{KNiFe}(\text{CN})_6$ (KNHCF) nanocubes on the surface of carbon nanotube fibers (CNTFs) by using nickel hydroxide as a nickel source, directly serving as the cathode (KNHCF@CNTF) for aqueous SIBs. As expected, the KNHCF@CNTF delivers a high volumetric capacity of $58.54 \text{ mAh cm}^{-3}$ at 0.05 A cm^{-3} and outstanding rate performance (72.7% retention after a 100-fold increase in current density), demonstrating a superfast charge–discharge characteristic.

Among various anode materials for SIBs, NTP, as a member of the NASICON family with an open framework and remarkable ionic conductivity, is considered as one of the most promising anode materials for SIBs because of its low cost and high theoretical capacity [40–45]. Despite these advantages,

the rate performance of NTP is limited by its poor electronic conductivity. High-temperature carbon coating, adopted in most of the previously reported studies, has been regarded as an effective method to overcome this issue [40, 41]. Unfortunately, this method is complex and involves harsh conditions. Herein, we synthesized rugby ball-shaped NTP on CNTFs by a one-step hydrothermal method and directly used them as electrodes (NTP@CNTF), exhibiting a high volumetric capacity (98.4 mAh cm^{-3} at 0.2 A cm^{-3}) and excellent rate performance (82.5% retention after a 40-fold increase in current density).

As a proof-of-concept demonstration, we employ KNHCF@CNTF and NTP@CNTF binder-free electrodes to successfully fabricate the first paradigm of a quasi-solid-state FARSIB. Benefiting from the remarkable performance of the binder-free electrodes, the device delivers a high capacity of $34.21 \text{ mAh cm}^{-3}$ and impressive energy density of $39.32 \text{ mWh cm}^{-3}$.

2 Experimental Section

2.1 Preparation of KNHCF@CNTF

KNHCF@CNTF was prepared by a simple chemical bath deposition and subsequent chemical etching process. CNTFs were cleaned with ethanol and deionized water. After being dried at $70 \text{ }^\circ\text{C}$ overnight, the CNTFs were pretreated in O_2 plasma for 8 min at 150 W. Firstly, 10 g of $\text{NiSO}_4 \cdot 6\text{H}_2\text{O}$ and 2 g $\text{K}_2\text{S}_2\text{O}_8$ were dissolved in 100 mL of H_2O under magnetic stirring and 5 mL aqueous ammonia (28%) was added into the above solution. Then, the pretreated CNTFs were suspended into the reaction for 40 min under slowly stirring. After that, the obtained CNTFs were washed repeatedly with distilled water and dried at $60 \text{ }^\circ\text{C}$ to get $\text{Ni}(\text{OH})_2$ @CNTFs. Next, the obtained $\text{Ni}(\text{OH})_2$ @CNTFs were placed in a solution of potassium ferricyanide at a certain concentration (1.5, 3.0, and 6.0 mM) for 24 h at room temperature. Finally, the KNHCF@CNTFs were cleaned with deionized water and dried at $60 \text{ }^\circ\text{C}$ in a vacuum for 12 h. The mass loading of active material on the surface of CNTF (3.0 mM) is about 2.42 mg cm^{-2} . For comparison, the powder of KNHCF was obtained by the same method. $\text{Ni}(\text{OH})_2$ powder (100 mg) and excess potassium ferricyanide were mixed under continuous magnetic stirring at room temperature. After 24 h, the reaction products were collected by centrifugation and washed several times with deionized water. Finally, the KNHCF powder was obtained after vacuum drying at $60 \text{ }^\circ\text{C}$ overnight.

2.2 Preparation of NTP@CNTF

NTP@CNTF was prepared by a simple and mild solvothermal method. CNTFs were cleaned and dried as described above. Firstly, 1 mL of TiCl_3 solution (30 wt% HCl) was dropwise added into 30 mL of ethylene glycol under string and kept stirring for 0.5 h. Then, 1 mL of phosphoric acid was dropwise added into the above solution. Next, 1 g of $\text{NaH}_2\text{PO}_4 \cdot 2\text{H}_2\text{O}$ was added into it. After stirring for 0.5 h, the reaction solution and pretreated CNTFs were placed into a 50-mL reaction vessel to heat at $150 \text{ }^\circ\text{C}$ for 6 h. Finally, the obtained NTP@CNTFs were rinsed with ethanol and distilled water and dried at $80 \text{ }^\circ\text{C}$ for 24 h. The mass loading of active material on the surface of CNTF is about 2.7 mg cm^{-2} . For comparison, the powder product in Teflon-lined stainless autoclave was collected by centrifugation and washed several times with deionized water and ethanol. After dried at $60 \text{ }^\circ\text{C}$ for 12 h, 0.1 g of obtained powder was added into 50 mL of glucose solution (0.04 M) under magnetic stirring. After stirring for 24 h, the glucose-coated NTP powders were collected by centrifugation and dried at $60 \text{ }^\circ\text{C}$ overnight. Finally, the NTP@C was obtained after annealing at $600 \text{ }^\circ\text{C}$ for 4 h in air atmosphere.

3 Results and Discussion

The fabrication procedure of the quasi-solid-state FARSIB is schematically represented in Fig. 1. First, KNHCF nanocubes were synthesized on the surface of CNTFs directly as a binder-free cathode via chemical bath deposition and subsequent chemical etching. The specific reaction process

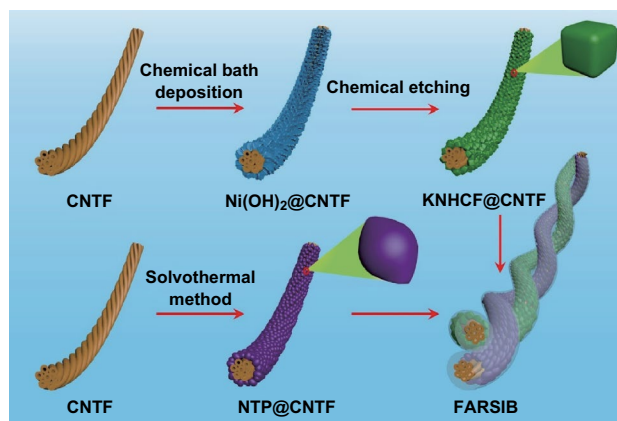


Fig. 1 Schematic illustration of the fabrication process of the quasi-solid-state FARSIB

is explained in Scheme S1. Simultaneously, the rugby ball-shaped NTP was grown on CNTFs by a mild solvothermal reaction to serve as an advanced anode for the FARSIB. Thereafter, both the as-fabricated KNHCF@CNTF and NTP@CNTF were immersed in a gel electrolyte consisting of Na_2SO_4 and carboxymethyl cellulose sodium (CMC) for a period of time and dried to form a thin layer of gel electrolyte. Finally, the quasi-solid-state FARSIB was fabricated by twisting the cathode and anode together.

3.1 Morphology and Structure of the Cathode Materials

The scanning electron microscopy (SEM) image (Fig. 2a) exhibits a CNTF with a uniform diameter of about 100 μm ,

which is composed of intertwined carbon nanotubes. In Fig. 2b, c, the SEM images show that $\text{Ni}(\text{OH})_2$ nanosheet arrays were uniformly coated on the surface of the CNTF by the simple chemical bath deposition method. After chemical etching, the nanosheet arrays are transformed into nanocubes with large porous gaps (Fig. 2d). The internal free space can not only promote the diffusion of electrolyte ions for better rate performance, but also accommodate the volume change of the electrode materials during intercalation and deintercalation of alkali cations, resulting in long cycle life and high specific capacity. It is noted that the fiber-shaped electrode still maintains an admirable tensile strength of about 300 MPa after the active materials are coated on its surface (Fig. S1), which is of great significance for the application of fiber-shaped energy-storage devices. The morphology of a nanocube with a side

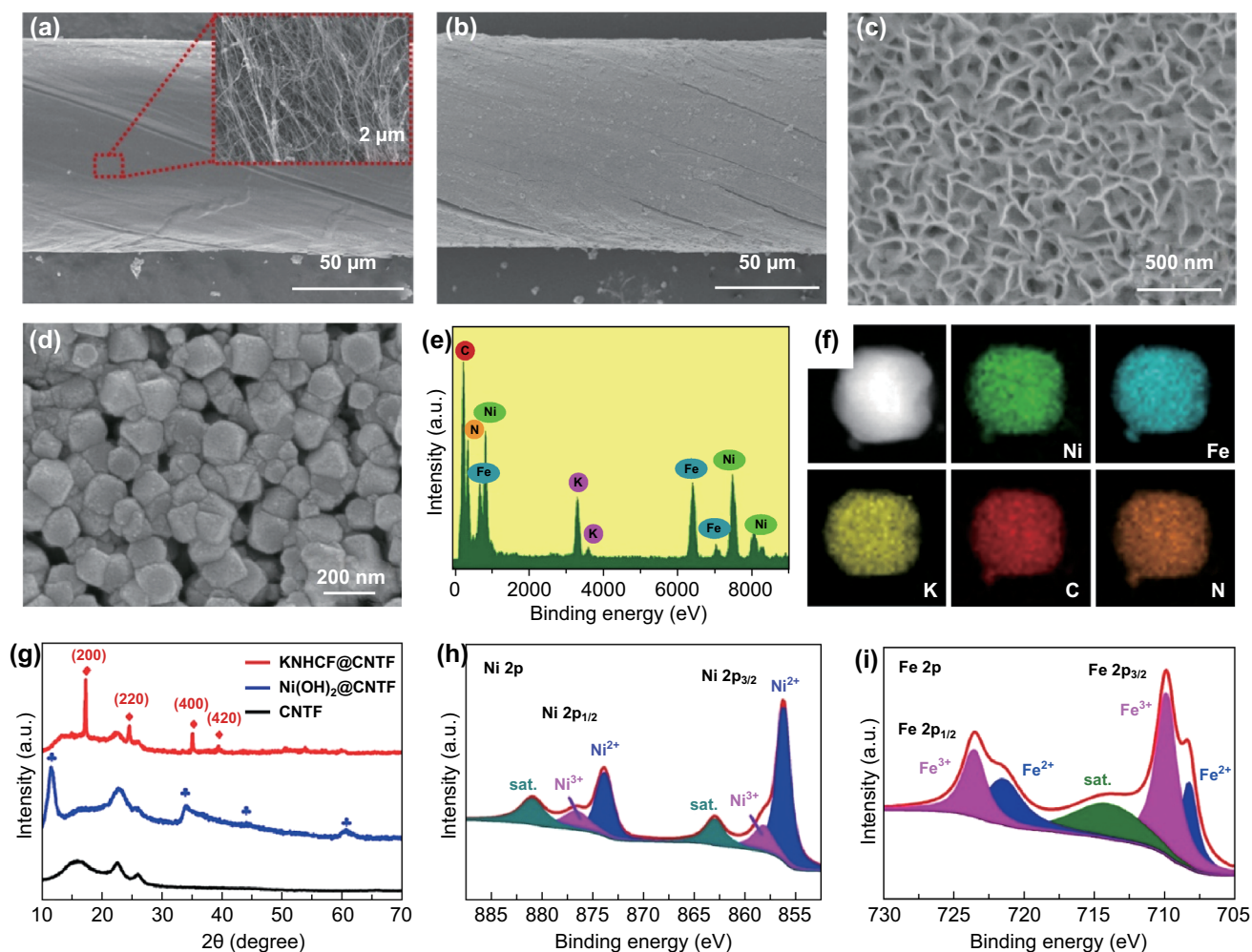


Fig. 2 SEM images of **a** pristine CNTF, **b**, **c** $\text{Ni}(\text{OH})_2$ @CNTF, and **d** KNHCF@CNTF. **e** EDS spectrum of KNHCF cube and **f** corresponding elemental mappings. **g** XRD patterns of KNHCF@CNTF, $\text{Ni}(\text{OH})_2$ @CNTF, and pristine CNTF; XPS survey scan of **h** Ni 2p and **i** Fe 2p

length of about 160 nm was further investigated by low-resolution transmission electron microscopy (TEM), as displayed in Fig. S2. Figure 2e, f exhibits the energy-dispersive spectroscopy (EDS) spectrum and elemental mapping, suggesting the coexistence and homogeneous distribution of the elements K, Ni, Fe, C, and N. To study the effect of the concentration of potassium ferricyanide solution on morphology, SEM images of the corresponding products at various concentrations are shown in Fig. S3. As the concentration of the reaction solution increases, the nanocubes gradually tend toward regular cube shapes, whereas the free space between the cubes gradually decreases.

More evidence for the conversion of $\text{Ni}(\text{OH})_2$ to KNHCF was obtained by X-ray diffraction (XRD). As shown in Fig. 2g, the characteristic peaks of the obtained nanosheets on CNTFs can all be indexed to those of $\alpha\text{-Ni}(\text{OH})_2$ (JCPDS No. 38-0715) except for the background peaks of the CNTFs themselves. After chemical etching, the characteristic peaks located at 17.3° , 24.5° , 35.0° , and 39.3° are consistent with the (200), (220), (400), and (420) phases of KNHCF, while the peaks of $\text{Ni}(\text{OH})_2$ disappear, implying that the $\text{Ni}(\text{OH})_2$ nanosheets are converted to KNHCF nanocubes. Figure S4 exhibits the X-ray photoelectron spectroscopy (XPS) survey spectra, further demonstrating the coexistence of the elements

K, Ni, Fe, C, and N. The high-resolution Ni 2p XPS spectrum (Fig. 2h) exhibits two main peaks located at 856.4 and 874.0 eV, respectively, consistent with the Ni $2p_{3/2}$ and Ni $2p_{1/2}$ states of Ni^{2+} , respectively [37]. In addition, the Fe 2p spectrum (Fig. 2i) of KNHCF contains two main peaks located at 709.8 and 723.6 eV, corresponding to those previously reported for Fe^{3+} [46].

3.2 Electrochemical Characterization of the Cathode Materials

Benefiting from the absence of conductive additives and binders, the cathode material for the ARSIBs was expected to display more efficient charge transfer and ion diffusion. The galvanostatic charge–discharge (GCD) curves at 0.05 A cm^{-3} of KNHCF@CNTF generated under different concentrations of the reaction solution are shown in Fig. S5, indicating that the volumetric capacity of KNHCF@CNTF is the maximum when the concentration is 3.0 mM. Figure 3a displays the cyclic voltammetry (CV) curves of $\text{Ni}(\text{OH})_2$ @CNTF, KNHCF powders, and KNHCF@CNTF at 5 mV s^{-1} . Evidently, the $\text{Ni}(\text{OH})_2$ @CNTF exhibits much less coverage than that of KNHCF@CNTF, implying that the untreated

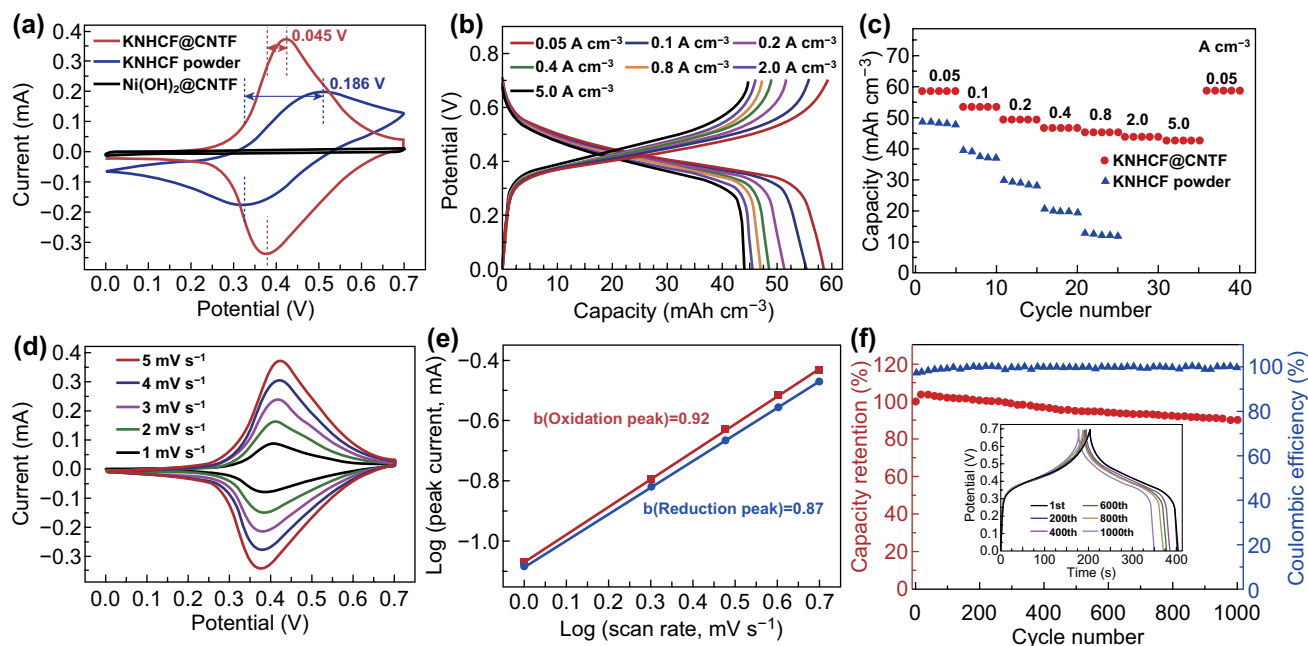


Fig. 3 **a** Comparison of CV curves of $\text{Ni}(\text{OH})_2$ @CNTF, KNHCF powder, and KNHCF@CNTF at a scan rate of 5 mV s^{-1} . **b** GCD curves of KNHCF@CNTF at various current densities from 0.05 to 5.0 A cm^{-3} . **c** Comparison of rate performance of KNHCF powder and KNHCF@CNTF. **d** CV curves at various scan rates, **e** corresponding b value, and **f** long-term cycle stability at 0.8 A cm^{-3} of the KNHCF@CNTF

Ni(OH)₂@CNTF is virtually incapable of storing and releasing sodium ions. As revealed in Fig. S6, the pristine CNTF just provides little contribution to the volumetric capacity. In addition, compared with KNHCF powder, the KNHCF@CNTF shows a much lower voltage hysteresis of 0.045 V and higher current, suggesting its faster reaction kinetics and larger capacity, which is further verified by the GCD curves at 0.05 A cm⁻³ (Fig. S7) [11, 47]. As shown in Fig. 3b, the GCD curves at various current densities displayed a stable output voltage plateau of about 0.4 V. It is worth mentioning that the KNHCF@CNTF electrode displays negligible voltage hysteresis at a range from 0.05 to 5.0 A cm⁻³ and only required 21.1 s per discharge or charge at a large current density of 5.0 A cm⁻³, indicating its superfast charge–discharge characteristic. More importantly, benefiting from the fast reaction kinetics, the KNHCF@CNTF electrode achieves a greater volumetric capacity (58.54 mAh cm⁻³ at 0.05 A cm⁻³) and better rate performance (72.7% retention after a 100-fold increase in current density), whereas the KNHCF powder electrode possesses a small volumetric capacity of 48.60 mAh cm⁻³ at the same current density [calculated from the corresponding GCD curves (Fig. S8)] and poor capacity retention of 25.5% when the current density increases to 0.8 A cm⁻³ (Fig. 3c). Such improved rate performance was demonstrated by the electrochemical impedance spectroscopy measurement (Fig. S9). For KNHCF@CNTF, the diameter of the semicircle in the high-frequency region was smaller and the slope of the line in the low-frequency region was greater than that of KNHCF powder, corresponding to better electron conductivity and ion diffusion [11, 48]. This demonstrates that the direct growth of active materials on the conductive substrates is beneficial to the electron transport and ion diffusion. The long-term cyclability of the KNHCF@CNTF was investigated at 0.8 A cm⁻³, and an excellent capacity of 52.85 mAh cm⁻³ was retained after 1000 cycles (Fig. 3f), with a low volumetric capacity decay of only 9.8% and high coulombic efficiency of about 100%, exhibiting outstanding cycle stability and reaction reversibility. The SEM images (Fig. S10) reveal that the free-standing nanocubes with a porous structure are still preserved even after long-term Na⁺ (de)intercalation (500 and 1000 cycles, 0.8 A cm⁻³), further indicating the remarkable structural stability.

Electrochemical kinetic analysis was performed by plotting CV curves to gain further insight into the Na⁺ storage process. Figure 3d shows the CV curves of the KNHCF@CNTF cathode measured at different scan rates from 1.0 to

5.0 mV s⁻¹, in which two nearly symmetric redox peaks correspond to the intercalation/extraction of Na⁺ in the KNHCF lattice. The proportion of diffusion-controlled and capacitive contributions can be described by Eq. 1 [49, 50]:

$$i = av^b \quad (1)$$

where values of b close to 0.5 and 1.0 correspond to diffusion-controlled and capacitive behavior, respectively. The values of b calculated from the redox peaks are 0.92 and 0.87, respectively, implying a capacitor-like process for the storage of Na⁺. In addition, the percentages of capacitive and diffusion-controlled contributions can be calculated by Eqs. 2 and 3 [51, 52]:

$$i = k_1v + k_2v^{1/2} \quad (2)$$

$$i/v^{1/2} = k_1v^{1/2} + k_2 \quad (3)$$

in which k_1 and k_2 are constants. Figure S11 exhibits the percentage contributions of the two kinetic processes at various scan rates. The contributions of the capacitive process are 76.7%, 81.4%, 84.4%, 86.7%, and 87.8% as the scan rates are increased from 1.0 to 5.0 mV s⁻¹. Based on the above analysis, the large contribution of capacitive behavior can be responsible for the superfast charge–discharge characteristic and excellent rate performance [50].

To gain insight into the structural evolution of the KNHCF cathode during the charge–discharge process, ex situ XRD and XPS were performed in various states of Na⁺ extraction/insertion (Fig. S12). Clearly, no new characteristic diffraction peaks appear, suggesting that the charge–discharge process belongs to a solid-solution reaction without the formation of a new phase [51]. Moreover, the characteristic (200) and (400) peaks slightly shift to larger angles with the insertion of Na⁺ and returned to their original position after the subsequent charging process, suggesting that the insertion of Na⁺ can lead to a volume decrease in the unit cell. This phenomenon is attributed to the attractive interactions of the inserted Na⁺ with the surrounding C≡N groups [53]. In addition, Fig. S13 displays the Na 2p and Fe 2p XPS regions for the fully charged and discharged states. In the Na 2p region, there is no intensity at the initial or the fully charged states, but a peak appears at 1072.3 eV during the discharge process, implying the highly reversible insertion/release of sodium in the host material during the discharge/charge process. To further explore the storage mechanism of sodium ions, the valence states of Fe were measured in various states. Figure S13b shows the Fe 2p XPS regions at the initial state, in which the main peaks

at 709.8 and 723.6 eV correspond to the Fe 2p_{3/2} and Fe 2p_{1/2} states of Fe³⁺, respectively. After being discharged to 0 V, the location of the main peak transfers to 708.5 eV, indicating that Fe³⁺ was reduced to Fe²⁺ upon the insertion of sodium ions (Fig. S13a). The main peak then returns to its initial location after the subsequent charging process, further demonstrating the excellent reversibility. Based on the above analysis, the reversible electrochemical reaction of sodium insertion and extraction in the cathode material can be depicted as: $x\text{Na}^+ + \text{KNi}[\text{Fe}(\text{CN})_6] + xe^- \leftrightarrow \text{Na}_x\text{KNi}[\text{Fe}(\text{CN})_6]$.

3.3 Morphology and Structure of the Anode Materials

As a high-performance anode material, rugby ball-shaped NTP was synthesized by a one-step solvothermal reaction on CNTFs. The SEM images in Fig. 4a, b show the surface of a CNTF uniformly coated by microparticles. The TEM image (Fig. 4c) reveals that the single active material consisted of rugby ball-shaped micron-scale particles with sizes of about

1 μm. The high-resolution TEM (HRTEM) image (Fig. 4d) reflects the high crystallinity of the rugby ball-shaped NTP, wherein the lattice fringe spacing of 0.37 nm corresponds to its (113) plane. The EDS spectrum (Fig. 4e) and its corresponding EDS mapping images (Fig. 4g) distinctly demonstrate the coexistence and uniform spatial distribution of Na, Ti, P, and O elements. XRD measurement was carried out to further confirm the composition and structure (Fig. 4f), in which all characteristic peaks are indexed to NTP (JCPDS No. 01-085-2265). The successful synthesis of NTP was likewise verified by XPS as shown in Fig. S14, the results of which were consistent with those of XRD and TEM. For comparison, carbon-coated NTP powders (NTP@C) were prepared and investigated by SEM and TEM (Fig. S15). The SEM and TEM images (Fig. S15a, b) show that the NTP@C powder retained the rugby ball-shaped structure. The HRTEM image (Fig. S15c) clearly shows that the NTP surface is uniformly coated with an amorphous carbon shell with a thickness of about 4 nm, forming a core-shell structure.

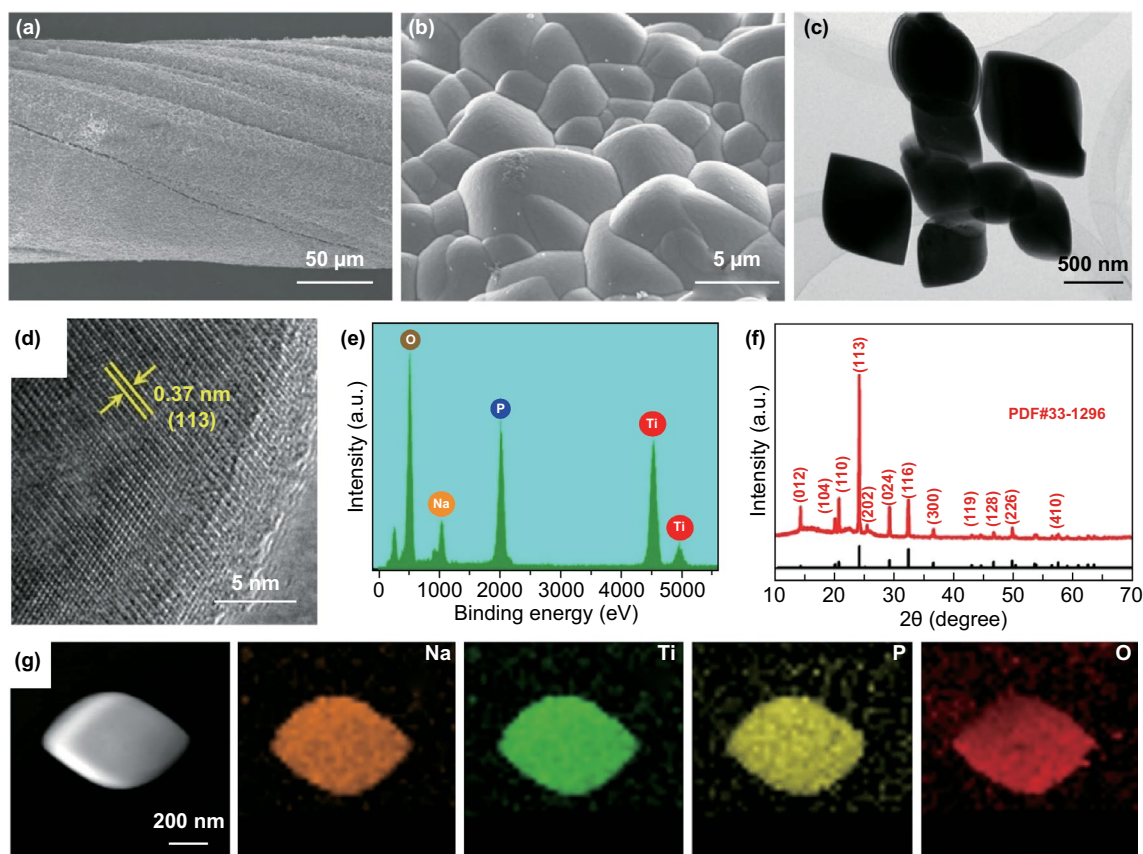


Fig. 4 a, b SEM images of NTP@CNTF with different magnifications. c, d TEM images at various magnifications, and e EDS spectrum of NTP. f XRD pattern of NTP@CNTF. g EDS element mappings for Na, Ti, P, and O of NTP

3.4 Electrochemical Characterization of the Anode Materials

The electrochemical properties of the obtained NTP@CNTF were investigated in a three-electrode system under the same conditions as for the cathode. Figure 5a compares the CV curves of pristine CNTF, NTP powder, NTP@C powder, and NTP@CNTF measured at 2 mV s^{-1} . Like the positive electrode, pristine CNTFs make little contribution to the volumetric capacity. In addition, compared with the NTP and NTP@C powders (same active materials loading with NTP@CNTF), the NTP@CNTF owns smaller separation of the redox peaks and a larger coverage area, indicating its smaller polarization and higher reversible capacity, which is further verified by their GCD curves at 1.6 A cm^{-3} (Fig. S16). As shown in Fig. 5b, the CV curves of NTP@CNTF measured at various scan rates show a pair of sharp redox peaks, corresponding to the characteristic potentials of a $\text{Ti}^{3+}/\text{Ti}^{4+}$ redox couple [54]. Figure 5c shows that the b values corresponding to the redox peaks are 0.76 and 0.71, respectively, from which it may be assumed that the sodium storage is a combination of surface-controlled and diffusion-controlled processes [49]. The GCD curves (Fig. 5d) at various current densities demonstrate stable charge–discharge

plateaus of about $-0.85/-0.75 \text{ V}$, which is consistent with the CV results. Besides, Fig. 5e displays the specific capacities of NTP@CNTF at various current densities and its corresponding coulombic efficiency. Remarkably, the NTP@CNTF can achieve an excellent volumetric capacity of 98.4 mAh cm^{-3} at 0.2 A cm^{-3} and possess a high capacity retention of 82.5% as the current density increases to 8.0 mA cm^{-3} , suggesting remarkable rate performance. The high coulombic efficiency implies the high reversibility of sodium-ion intercalation and deintercalation at the anode material. The electrochemical impedance spectrum (Fig. S17) indicates the remarkable electronic conductivity and ion diffusivity of the anode. The long-term cycling stability of NTP@CNTF was also explored (Fig. 5f), with 87.6% retention after 3000 cycles at a current density of 4.0 mA cm^{-3} . As demonstrated in Fig. S18, the SEM images show that the free-standing rugby ball-shaped structure is well preserved after 1000 cycles and only partly disrupts even after 3000 cycles, suggesting strong adhesion between active material and CNTF. The outstanding electrochemical performance achieved in this work is superior to those of many previously reported NTP-based materials that require high-temperature heat treatment and binders (Table S1).

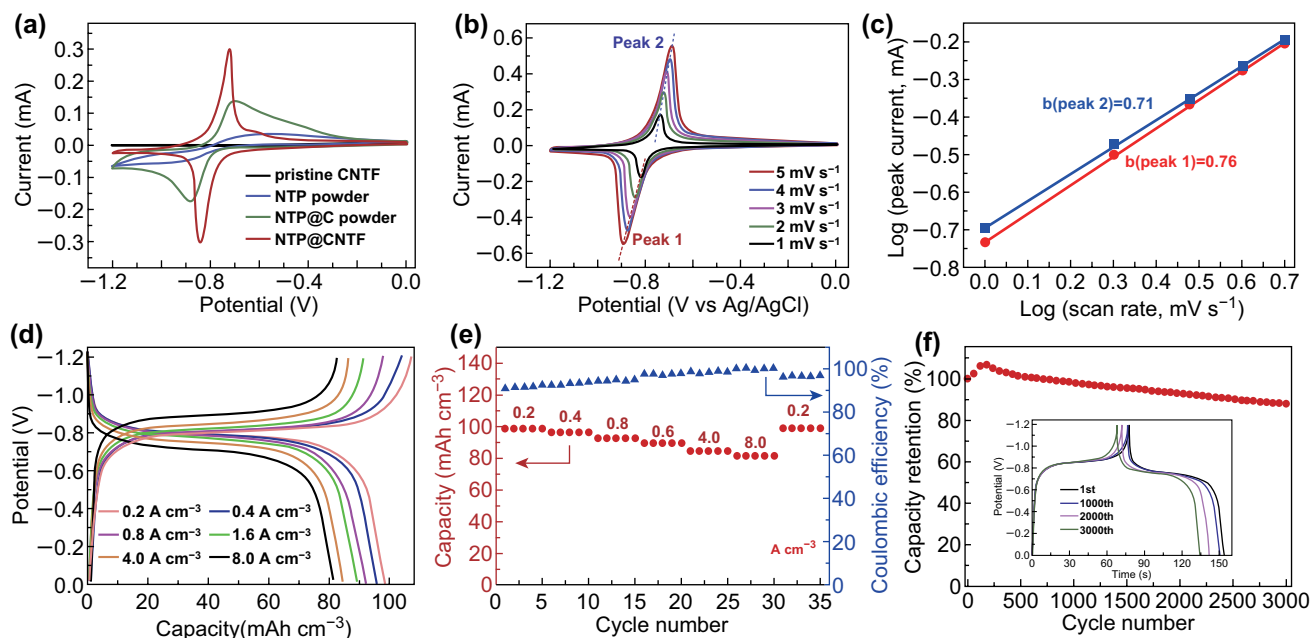


Fig. 5 **a** Comparison of the CV curves at 2 mV s^{-1} for NTP@CNTF, CNTF, NTP@C, and NTP powders. **b** CV curves and **c** the corresponding b value of NTP@CNTF at various scan rates from 1 to 5 mV s^{-1} . **d** GCD curves and **e** rate properties and coulombic efficiency of NTP@CNTF at various current densities from 0.2 to 8.0 mA cm^{-3} . **f** Cycle stability of NTP@CNTF at 4.0 A cm^{-3}

3.5 Electrochemical Performance and Flexibility Test of as-Prepared FARSIBs

Based on the above analysis, an aqueous Na-ion full cell was fabricated using KNHCF@CNTF and NTP@CNTF as the cathode and anode, respectively. To achieve charge balance between them, the length ratio of the cathode and anode is set at about 2:1. Figure S19 shows the corresponding CV curves at 5 mV s^{-1} . To verify the potential of the two binder-free electrodes for wearable energy-storage devices, a quasi-solid-state FARSIB was successfully assembled with a CMC- Na_2SO_4 polymer electrolyte. A low-resolution SEM image (Fig. S20) of the fiber-shaped device displayed a twisted structure. Figure 6a shows the CV curves of this FARSIB, all of which exhibit a pair of apparent redox peaks at various scan rates from 1 to 5 mV s^{-1} . The GCD curves (Fig. 6b) were measured at various current densities from 0.2 to 4.0 A cm^{-3} and displayed a stable discharge plateau of $\sim 1.15 \text{ V}$. Notably, the FARSIB delivers a volumetric capacity of $34.21 \text{ mAh cm}^{-3}$ at 0.2 A cm^{-3} and can retain a high capacity of $24.23 \text{ mAh cm}^{-3}$ at 4.0 A cm^{-3} , implying its remarkable rate properties. The long-term cycling stability and corresponding coulombic efficiency of the FARSIB were tested at 2.0 A cm^{-3} (Fig. 6c), still maintaining about

84.7% of initial capacity after 500 cycles and high coulombic efficiency close to 100%. The volumetric energy and power density of our FARSIB are displayed in Fig. 6d. The FARSIB reaches a maximum volumetric energy density of $39.32 \text{ mWh cm}^{-3}$ and a maximum volumetric power density of 4.60 W cm^{-3} , which considerably exceeded the values previously reported for other fiber-shaped energy-storage devices, such as Co//Zn battery [13], GO/MWCNT// MoS_2 -rGO/MWCNT [55], Ni//Zn battery [11], NiCo//Zn battery [56], titanium wire/ Co_3O_4 nanowires//carbon fibers/graphene [57], and NIB [5]. In addition, based on the total mass of the fiber-shaped cathode and anode (including active and inactive components), the specific energy/power densities were calculated as shown in Fig. S21. Thanks to the lightweight CNTFs, the assembled FARSIB exhibits a maximum specific energy density of about 27.72 Wh kg^{-1} and still maintains a high specific energy density of about 19.61 Wh kg^{-1} achieving a maximum power density of about 3.24 KW kg^{-1} . For fiber-shaped energy-storage devices, mechanical flexibility is of great significance for practical application as a power source for wearable electronic devices. As shown in Fig. 6e, there are negligible changes in capacity at 1.2 A cm^{-3} under various bending angles, exhibiting the excellent mechanical flexibility of the assembled device. Furthermore, the full

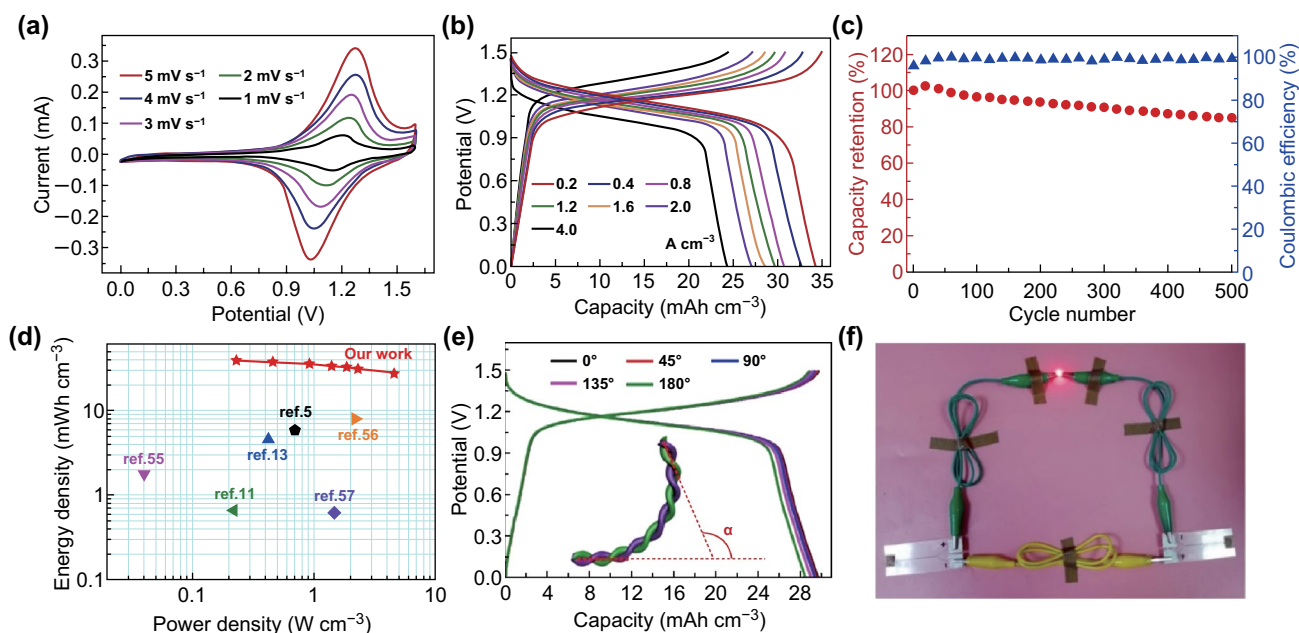


Fig. 6 **a** CV curves at various scan rates from 1 to 5 mV s^{-1} , **b** GCD curves at various current densities from 0.2 to 4.0 A cm^{-3} , **c** cycle stability and corresponding coulombic efficiency at 2.0 A cm^{-3} , and **d** Ragone plot of the quasi-solid-state FARSIB with a CMC- Na_2SO_4 polymer electrolyte. **e** GCD curves of the FARSIB at various bending angles. **f** LED powered by two FARSIBs in series

battery exhibits superior mechanical stability with only 5.7% of initial capacity loss after bending at 90° for 3000 cycles (Fig. S22), which can be attributed to the absence of binders and strong adhesion between the active materials and CNTF. Figure S23 exhibits the electrochemical impedance spectroscopies of the assembled FARSIB before and after bending tests, indicating the slight increase in the contact resistance (R_s) and faradic charge-transfer resistance (R_{ct}) of the electrodes after the bending test. In addition, an LED could be powered by two of the assembled fiber-shaped batteries connected in series (Fig. 6f), and the brightness of the LED barely changed when the devices were bent at various angles (Fig. S24). To further demonstrate the potential of the FARSIBs in wearable electronics, two assembled FARSIBs were woven into the flexible textile with an abbreviation (NB) of “Na-ion battery” and powered for a red LED shown in Fig. S25, verifying the practicability and high flexibility of our FARSIBs.

4 Conclusion

In summary, a prototype FARSIB was fabricated for the first time by growing nanocube-like KNHCF and rugby ball-shaped NTP on CNTFs directly as the cathode and anode, respectively. Benefiting from the absence of binders, both the cathode and anode exhibit remarkable electronic conductivity and ionic diffusion, accordingly delivering excellent capacities and rate performance. More encouragingly, the assembled quasi-solid-state fiber-shaped SIB could achieve a high capacity of 34.21 mAh cm⁻³ and impressive energy density of 39.32 mWh cm⁻³. Furthermore, due to the strong adhesion between the active materials and CNTFs, the capacity of our devices barely decayed when bent at a range of angles, displaying admirable mechanical flexibility. Thus, this work may be a stepping stone toward the development of all binder-free electrodes for next-generation wearable ARSIBs.

Acknowledgements This work was supported by the Fundamental Research Funds for the Central Universities (No. 020514380183), the National Natural Science Foundation of China (No. 51703241), the Key Research Program of Frontier Science of Chinese Academy of Sciences (No. QYZDB-SSW-SLH031), the Thousand Youth Talents Plan, and the Science and Technology Project of Nanchang (2017-SJSYS-008).

Open Access This article is distributed under the terms of the Creative Commons Attribution 4.0 International License (<http://creativecommons.org/licenses/by/4.0/>), which permits unrestricted use, distribution, and reproduction in any medium, provided you give appropriate credit to the original author(s) and the source, provide a link to the Creative Commons license, and indicate if changes were made.

Electronic supplementary material The online version of this article (<https://doi.org/10.1007/s40820-019-0332-7>) contains supplementary material, which is available to authorized users.

References

1. F. Mo, G. Liang, Q. Meng, Z. Liu, H. Li, J. Fan, C. Zhi, A flexible rechargeable aqueous zinc manganese-dioxide battery working at -20°C. *Energy Environ. Sci.* **12**(2), 706–715 (2019). <https://doi.org/10.1039/C8EE02892C>
2. H. Li, C. Han, Y. Huang, Y. Huang, M. Zhu et al., An extremely safe and wearable solid-state zinc ion battery based on a hierarchical structured polymer electrolyte. *Energy Environ. Sci.* **11**(4), 941–951 (2018). <https://doi.org/10.1039/C7EE03232C>
3. Q. Xue, J. Sun, Y. Huang, M. Zhu, Z. Pei et al., Recent progress on flexible and wearable supercapacitors. *Small* **13**(45), 1701827 (2017). <https://doi.org/10.1002/sml.201701827>
4. C. Yang, X. Ji, X. Fan, T. Gao, L. Suo et al., Flexible aqueous Li-ion battery with high energy and power densities. *Adv. Mater.* **29**(44), 1701972 (2017). <https://doi.org/10.1002/adma.201701972>
5. Z. Guo, Y. Zhao, Y. Ding, X. Dong, L. Chen et al., Multifunctional flexible aqueous sodium-ion batteries with high safety. *Chem* **3**(2), 348–362 (2017). <https://doi.org/10.1016/j.chempr.2017.05.004>
6. Y. Zhang, Y. Jiao, L. Lu, L. Wang, T. Chen, H. Peng, An ultra-flexible silicon-oxygen battery fiber with high energy density. *Angew. Chem. Int. Ed.* **56**(44), 13741–13746 (2017). <https://doi.org/10.1002/anie.201707840>
7. Q. Zhang, W. Xu, J. Sun, Z. Pan, J. Zhao et al., Constructing ultrahigh-capacity zinc-nickel-cobalt oxide@Ni(OH)₂ core-shell nanowire arrays for high-performance coaxial fiber-shaped asymmetric supercapacitors. *Nano Lett.* **17**(12), 7552–7560 (2017). <https://doi.org/10.1021/acs.nanolett.7b03507>
8. Q. Zhang, C. Li, Q. Li, Z. Pan, J. Sun et al., Flexible and high-voltage coaxial-fiber aqueous rechargeable zinc-ion battery. *Nano Lett.* **19**(6), 4035–4042 (2019). <https://doi.org/10.1021/acs.nanolett.9b01403>
9. Q. Zhang, X. Wang, Z. Pan, J. Sun, J. Zhao et al., Wrapping aligned carbon nanotube composite sheets around vanadium nitride nanowire arrays for asymmetric coaxial fiber-shaped supercapacitors with ultrahigh energy density. *Nano Lett.* **17**(4), 2719–2726 (2017). <https://doi.org/10.1021/acs.nanolett.7b00854>

10. Q. Zhang, L. Li, H. Li, L. Tang, B. He et al., Ultra-endurance coaxial-fiber stretchable sensing systems fully powered by sunlight. *Nano Energy* **60**, 267–274 (2019). <https://doi.org/10.1016/j.nanoen.2019.03.049>
11. Y. Zeng, Y. Meng, Z. Lai, X. Zhang, M. Yu, P. Fang, M. Wu, Y. Tong, X. Lu, An ultrastable and high-performance flexible fiber-shaped Ni–Zn battery based on a Ni–NiO heterostructured nanosheet cathode. *Adv. Mater.* **29**(44), 1702698 (2017). <https://doi.org/10.1002/adma.201702698>
12. M. Yao, R. Wang, Z. Zhao, Y. Liu, Z. Niu, J. Chen, A flexible all-in-one lithium-sulfur battery. *ACS Nano* **12**(12), 12503–12511 (2018). <https://doi.org/10.1021/acsnano.8b06936>
13. M. Li, J. Meng, Q. Li, M. Huang, X. Liu, K.A. Owusu, Z. Liu, L. Mai, Finely crafted 3D electrodes for dendrite-free and high-performance flexible fiber-shaped Zn–Co batteries. *Adv. Funct. Mater.* **28**(32), 1802016 (2018). <https://doi.org/10.1002/adfm.201802016>
14. Y.-H. Zhu, X. Yang, D. Bao, X.-F. Bie, T. Sun et al., High-energy-density flexible potassium-ion battery based on patterned electrodes. *Joule* **2**(4), 736–746 (2018). <https://doi.org/10.1016/j.joule.2018.01.010>
15. Y. Shao, J. Li, Y. Li, H. Wang, Q. Zhang, R.B. Kaner, Flexible quasi-solid-state planar micro-supercapacitor based on cellular graphene films. *Mater. Horiz.* **4**(6), 1145–1150 (2017). <https://doi.org/10.1039/C7MH00441A>
16. J. Xu, J. Chen, S. Zhou, C. Han, M. Xu, N. Zhao, C.-P. Wong, Sequentially-processed $\text{Na}_3\text{V}_2(\text{PO}_4)_3$ for cathode material of aprotic sodium ion battery. *Nano Energy* **50**, 323–330 (2018). <https://doi.org/10.1016/j.nanoen.2018.05.015>
17. X. Xiang, K. Zhang, J. Chen, Recent advances and prospects of cathode materials for sodium-ion batteries. *Adv. Mater.* **27**(36), 5343–5364 (2015). <https://doi.org/10.1002/adma.201501527>
18. M. Lao, Y. Zhang, W. Luo, Q. Yan, W. Sun, S.X. Dou, Alloy-based anode materials toward advanced sodium-ion batteries. *Adv. Mater.* **29**(48), 1700622 (2017). <https://doi.org/10.1002/adma.201700622>
19. H. Xia, X. Zhu, J. Liu, Q. Liu, S. Lan et al., A monoclinic polymorph of sodium birnessite for ultrafast and ultrastable sodium ion storage. *Nat. Commun.* **9**(1), 5100 (2018). <https://doi.org/10.1038/s41467-018-07595-y>
20. H.-G. Wang, W. Li, D.-P. Liu, X.-L. Feng, J. Wang et al., Flexible electrodes for sodium-ion batteries: recent progress and perspectives. *Adv. Mater.* **29**(45), 1703012 (2017). <https://doi.org/10.1002/adma.201703012>
21. J.-Y. Hwang, H.-L. Du, B.-N. Yun, M.-G. Jeong, J.-S. Kim, H. Kim, H.-G. Jung, Y.-K. Sun, Carbon-free TiO_2 microspheres as anode materials for sodium ion batteries. *ACS Energy Lett.* **4**(2), 494–501 (2019). <https://doi.org/10.1021/acsenenergylett.8b02510>
22. H. Long, W. Zeng, H. Wang, M. Qian, Y. Liang, Z. Wang, Self-assembled biomolecular 1d nanostructures for aqueous sodium-ion battery. *Adv. Sci.* **5**(3), 1700634 (2018). <https://doi.org/10.1002/advs.201700634>
23. Y. Liu, Y. Qiao, W. Zhang, H. Xu, Z. Li et al., High-performance aqueous sodium-ion batteries with $\text{K}_{0.27}\text{MnO}_2$ cathode and their sodium storage mechanism. *Nano Energy* **5**, 97–104 (2014). <https://doi.org/10.1016/j.nanoen.2014.02.010>
24. H. Gao, J.B. Goodenough, An aqueous symmetric sodium-ion battery with NASICON-structured $\text{Na}_3\text{MnTi}(\text{PO}_4)_3$. *Angew. Chem. Int. Ed.* **55**(41), 12768–12772 (2016). <https://doi.org/10.1002/anie.201606508>
25. L. Suo, O. Borodin, Y. Wang, X. Rong, W. Sun et al., “Water-in-salt” electrolyte makes aqueous sodium-ion battery safe, green, and long-lasting. *Adv. Energy Mater.* **7**(21), 1701189 (2017). <https://doi.org/10.1002/aenm.201701189>
26. M.H. Lee, S.J. Kim, D. Chang, J. Kim, S. Moon et al., Toward a low-cost high-voltage sodium aqueous rechargeable battery. *Mater. Today* (2019). <https://doi.org/10.1016/j.mattoday.2019.02.004>
27. X. Dong, L. Chen, J. Liu, S. Haller, Y. Wang, Y. Xia, Environmentally-friendly aqueous Li (or Na)-ion battery with fast electrode kinetics and super-long life. *Sci. Adv.* **2**(1), 1501038 (2016). <https://doi.org/10.1126/sciadv.1501038>
28. T. Jin, Q. Han, L. Jiao, Binder-free electrodes for advanced sodium-ion batteries. *Adv. Mater.* (2018). <https://doi.org/10.1002/adma.201806304>
29. L. Xue, Q. Zhang, X. Zhu, L. Gu, J. Yue et al., 3D LiCoO_2 nanosheets assembled nanorod arrays via confined dissolution-recrystallization for advanced aqueous lithium-ion batteries. *Nano Energy* **56**, 463–472 (2019). <https://doi.org/10.1016/j.nanoen.2018.11.085>
30. C. Guan, X. Liu, W. Ren, X. Li, C. Cheng, J. Wang, Rational design of metal-organic framework derived hollow NiCo_2O_4 arrays for flexible supercapacitor and electrocatalysis. *Adv. Energy Mater.* **7**(12), 1602391 (2017). <https://doi.org/10.1002/aenm.201602391>
31. L. Xue, S.V. Savilov, V.V. Lunin, H. Xia, Self-standing porous LiCoO_2 nanosheet arrays as 3D cathodes for flexible Li-ion batteries. *Adv. Funct. Mater.* **28**(7), 1705836 (2018). <https://doi.org/10.1002/adfm.201705836>
32. Q. Zhang, Z. Zhou, Z. Pan, J. Sun, B. He et al., All-metal-organic framework-derived battery materials on carbon nanotube fibers for wearable energy-storage device. *Adv. Sci.* **5**(12), 1801462 (2018). <https://doi.org/10.1002/advs.201801462>
33. J. Han, H. Zhang, A. Varzi, S. Passerini, Fluorine-free water-in-salt electrolyte for green and low-cost aqueous sodium-ion batteries. *ChemSusChem* **11**(21), 3704–3707 (2018). <https://doi.org/10.1002/cssc.201801930>
34. K. Nakamoto, R. Sakamoto, Y. Sawada, M. Ito, S. Okada, Over 2 V aqueous sodium-ion battery with Prussian blue-type electrodes. *Small Methods* **3**(4), 1800220 (2019). <https://doi.org/10.1002/smt.201800220>
35. Z. Li, D. Young, K. Xiang, W.C. Carter, Y.-M. Chiang, Towards high power high energy aqueous sodium-ion batteries: the $\text{NaTi}_2(\text{PO}_4)_3/\text{Na}_{0.44}\text{MnO}_2$ system. *Adv. Energy Mater.* **3**(3), 290–294 (2013). <https://doi.org/10.1002/aenm.201200598>
36. W. Ren, M. Qin, Z. Zhu, M. Yan, Q. Li, L. Zhang, D. Liu, L. Mai, Activation of sodium storage sites in Prussian blue



- analogues via surface etching. *Nano Lett.* **17**(8), 4713–4718 (2017). <https://doi.org/10.1021/acs.nanolett.7b01366>
37. P. Ge, S. Li, H. Shuai, W. Xu, Y. Tian, L. Yang, G. Zou, H. Hou, X. Ji, Ultrafast sodium full batteries derived from xFe (x = Co, Ni, Mn) Prussian blue analogs. *Adv. Mater.* **31**(3), 1806092 (2019). <https://doi.org/10.1002/adma.201806092>
38. J. Qian, C. Wu, Y. Cao, Z. Ma, Y. Huang, X. Ai, H. Yang, Prussian blue cathode materials for sodium-ion batteries and other ion batteries. *Adv. Energy Mater.* **8**(17), 1702619 (2018). <https://doi.org/10.1002/aenm.201702619>
39. M. Pasta, C.D. Wessells, N. Liu, J. Nelson, M.T. McDowell, R.A. Huggins, M.F. Toney, Y. Cui, Full open-framework batteries for stationary energy storage. *Nat. Commun.* **5**, 3007 (2014). <https://doi.org/10.1038/ncomms4007>
40. P. Wei, Y. Liu, Z. Wang, Y. Huang, Y. Jin et al., Porous $\text{NaTi}_2(\text{PO}_4)_3/\text{C}$ hierarchical nanofibers for ultrafast electrochemical energy storage. *ACS Appl. Mater. Interfaces* **10**(32), 27039–27046 (2018). <https://doi.org/10.1021/acsami.8b08415>
41. L. Wang, Z. Huang, B. Wang, G. Liu, M. Cheng et al., Purifying the phase of $\text{NaTi}_2(\text{PO}_4)_3$ for enhanced Na^+ storage properties. *ACS Appl. Mater. Interfaces* **11**(11), 10663–10671 (2019). <https://doi.org/10.1021/acsami.9b00116>
42. Q. Yang, S. Cui, Y. Ge, Z. Tang, Z. Liu et al., Porous single-crystal $\text{NaTi}_2(\text{PO}_4)_3$ via liquid transformation of TiO_2 nanosheets for flexible aqueous Na-ion capacitor. *Nano Energy* **50**, 623–631 (2018). <https://doi.org/10.1016/j.nanoen.2018.06.017>
43. C. Wu, P. Kopold, Y.-L. Ding, P.A. van Aken, J. Maier, Y. Yu, Synthesizing porous $\text{NaTi}_2(\text{PO}_4)_3$ nanoparticles embedded in 3D graphene networks for high-rate and long cycle-life sodium electrodes. *ACS Nano* **9**(6), 6610–6618 (2015). <https://doi.org/10.1021/acs.nano.5b02787>
44. Q. Hu, J.-Y. Liao, C.-T. Li, X.-D. He, X. Ding, C.-H. Chen, Synthesis of porous carbon-coated $\text{NaTi}_2(\text{PO}_4)_3$ nanocubes with a high-yield and superior rate properties. *J. Mater. Chem. A* **6**(47), 24503–24508 (2018). <https://doi.org/10.1039/C8TA10182E>
45. B. Zhao, B. Lin, S. Zhang, C. Deng, A frogspawn-inspired hierarchical porous $\text{NaTi}_2(\text{PO}_4)_3\text{-C}$ array for high-rate and long-life aqueous rechargeable sodium batteries. *Nanoscale* **7**(44), 18552–18560 (2015). <https://doi.org/10.1039/C5NR06505D>
46. F.-C. Zhou, Y.-H. Sun, J.-Q. Li, J.-M. Nan, $\text{K}_{1-x}\text{Mn}_{1+x/2}[\text{Fe}(\text{CN})_6] \cdot y\text{H}_2\text{O}$ Prussian blue analogues as an anode material for lithium-ion batteries. *Appl. Surf. Sci.* **444**, 650–660 (2018). <https://doi.org/10.1016/j.apsusc.2018.03.102>
47. Y. Zhang, Y. Wang, L. Wang, C.-M. Lo, Y. Zhao, Y. Jiao, G. Zheng, H. Peng, A fiber-shaped aqueous lithium ion battery with high power density. *J. Mater. Chem. A* **4**(23), 9002–9008 (2016). <https://doi.org/10.1039/C6TA03477B>
48. Y. Song, T. Liu, B. Yao, M. Li, T. Kou et al., Ostwald ripening improves rate capability of high mass loading manganese oxide for supercapacitors. *ACS Energy Lett.* **2**(8), 1752–1759 (2017). <https://doi.org/10.1021/acsenergylett.7b00405>
49. C. Xia, J. Guo, Y. Lei, H. Liang, C. Zhao, H.N. Alshareef, Rechargeable aqueous zinc-ion battery based on porous framework zinc pyrovanadate intercalation cathode. *Adv. Mater.* **30**(5), 1705580 (2018). <https://doi.org/10.1002/adma.201705580>
50. B. Tang, G. Fang, J. Zhou, L. Wang, Y. Lei, C. Wang, T. Lin, Y. Tang, S. Liang, Potassium vanadates with stable structure and fast ion diffusion channel as cathode for rechargeable aqueous zinc-ion batteries. *Nano Energy* **51**, 579–587 (2018). <https://doi.org/10.1016/j.nanoen.2018.07.014>
51. D. Chao, C. Zhu, M. Song, P. Liang, X. Zhang et al., A high-rate and stable quasi-solid-state zinc-ion battery with novel 2D layered zinc orthovanadate array. *Adv. Mater.* **30**(32), 1803181 (2018). <https://doi.org/10.1002/adma.201803181>
52. Y. Li, Z. Huang, P.K. Kalambate, Y. Zhong, Z. Huang, M. Xie, Y. Shen, Y. Huang, V_2O_5 nanopaper as a cathode material with high capacity and long cycle life for rechargeable aqueous zinc-ion battery. *Nano Energy* **60**, 752–759 (2019). <https://doi.org/10.1016/j.nanoen.2019.04.009>
53. M.S. Chae, J.W. Heo, H.H. Kwak, H. Lee, S.-T. Hong, Organic electrolyte-based rechargeable zinc-ion batteries using potassium nickel hexacyanoferrate as a cathode material. *J. Power Sources* **337**, 204–211 (2017). <https://doi.org/10.1016/j.jpowsour.2016.10.083>
54. G. Pang, P. Nie, C. Yuan, L. Shen, X. Zhang, J. Zhu, B. Ding, Enhanced performance of aqueous sodium-ion batteries using electrodes based on the $\text{NaTi}_2(\text{PO}_4)_3/\text{MWNTs-Na}_{0.44}\text{MnO}_2$ system. *Energy Technol.* **2**(8), 705–712 (2014). <https://doi.org/10.1002/ente.201402045>
55. G. Sun, X. Zhang, R. Lin, J. Yang, H. Zhang, P. Chen, Hybrid fibers made of molybdenum disulfide, reduced graphene oxide, and multi-walled carbon nanotubes for solid-state, flexible, asymmetric supercapacitors. *Angew. Chem. Int. Ed.* **54**(15), 4651–4656 (2015). <https://doi.org/10.1002/anie.201411533>
56. Y. Huang, W.S. Ip, Y.Y. Lau, J. Sun, J. Zeng et al., Weavable, conductive yarn-based NiCo//Zn textile battery with high energy density and rate capability. *ACS Nano* **11**(9), 8953–8961 (2017). <https://doi.org/10.1021/acs.nano.7b03322>
57. X. Wang, B. Liu, R. Liu, Q. Wang, X. Hou, D. Chen, R. Wang, G. Shen, Fiber-based flexible all-solid-state asymmetric supercapacitors for integrated photodetecting system. *Angew. Chem. Int. Ed.* **53**(7), 1849–1853 (2014). <https://doi.org/10.1002/anie.201307581>